SCIENCE CHINA
Information Sciences

• RESEARCH PAPER •
Special Focus on Geosynchronous Synthetic Aperture Radar

June 2017, Vol. 60 060308:1–060308:13
doi: 10.1007/s11432-016-9064-1

L-band geosynchronous SAR imaging degradations imposed by ionospheric irregularities

Yifei JI, Qilei ZHANG*, Yongsheng ZHANG & Zhen DONG

College of Electronic Science and Engineering, National University of Defense Technology, Changsha 410073, China

Received February 17, 2017; accepted March 29, 2017; published online May 16, 2017

Abstract It is well known that the ionospheric scintillation caused by small-scale ionospheric irregularities is a major distortion source for low-frequency spaceborne synthetic aperture radar (SAR) imaging. For L-band geosynchronous earth orbit (GEO) SAR, the orbit height is ultra-high and the integration time is ultra-long, thus ionospheric irregularities may cause more significant distortions on the imaging focusing. To evaluate this effect, the generalized ambiguity function (GAF) is employed to establish the analytical model. The imaging resolution can be studied by calculating the second moment of GAF. Furthermore, since the scanning velocity of the ionospheric penetration point (IPP) for GEO SAR is much slower than that of low earth orbit (LEO) SAR, the convection velocity of the ionospheric irregularities is no longer negligible. Taking this into account, we derive a more accurate expression of ionospheric irregularities' effect. The theoretical derivation is validated by numerical analyses and signal-level simulations.

Keywords ionospheric irregularities, L-band GEO SAR, generalized ambiguity function, imaging resolution, convection velocity

Citation Ji Y F, Zhang Q L, Zhang Y S, et al. L-band geosynchronous SAR imaging degradations imposed by ionospheric irregularities. Sci China Inf Sci, 2017, 60(6): 060308, doi: 10.1007/s11432-016-9064-1

1 Introduction

There has been a promising trend in the use of geosynchronous synthetic aperture radar (GEO SAR), for realizing a wide-coverage monitoring within a shorter revisit time [1–9]. It usually works at L-band, where it may suffer the marked influence of the dispersive and random ionospheric medium, which can be generally categorized into the background ionosphere with macroscopic scales greater than several hundred kilometers, and the ionospheric irregularities on scales from a few meters to a few tens of kilometers [10,11]. The former will cause refraction, dispersion, group delay, phase advance, and Faraday rotation [10–12]. The latter is known as ionospheric scintillation and generated by the turbulent plasmas, which act remarkably in the polar cap and equatorial zone at night [13–19]. Therefore, it is important to evaluate potential effects and devise mitigation techniques before launching an L-band GEO SAR satellite [20–25]. Effects of the temporal-variable background ionosphere on GEO SAR imaging were particularly specified by using polynomial approximation of the measured data of the total electron

* Corresponding author (email: zhangqilei@nudt.edu.cn)

content (TEC) [20, 21]. Meanwhile, analyses of the GEO SAR imaging in the presence of ionospheric scintillation were performed via theoretical derivations and validated by using external measurement devices [22–25]. These constructive achievements lay a solid foundation for our research. Nevertheless, some special and significant problems have not yet been recognized and studied, which are under our research in this paper.

Ionospheric effects on the P-band spaceborne SAR imaging were well encompassed and preliminarily analyzed with the generalized ambiguity function (GAF), including the dispersion, ionospheric turbulence and Faraday rotation [26]. On the basis of GAF, numbers of theoretical and numerical analyses was also well performed [27–30]. In [28], the two-frequency and two-position coherence function (TFTPCF) was introduced to present a proper description of ionospheric irregularities, for both azimuth and range resolution; it was concluded that ionospheric effects caused by dispersive irregularities could decrease the signal bandwidth and the coherent length. However, these analytical models are not yet well applied to the L-band GEO SAR system. And then, corresponding analyses will be presented in this paper.

For the LEO SAR system, the ionospheric turbulence is generally assumed to be time independent, since the integration time is quite short [17, 18, 28]. However, in practice the ionospheric fluctuation is a space-time field. Even for the "frozen field" assumption, the ionospheric turbulence convection exists. It was reported that the convection velocity of the ionospheric irregularities was up to 100 m/s in the equatorial region [17]. For GEO SAR, since the orbit altitude is ultra-high, the IPP scanning velocity, which is much lower than that of the LEO SAR, is comparable with the convection velocity of the ionospheric irregularities. Moreover, the convection distance during the ultra-long integration time of GEO SAR is considerable. This means that the effect of the flowing ionospheric irregularities on the GEO SAR imaging focusing needs to be considered.

The aim of this paper is to provide a comprehensive analysis to evaluate effects of the ionospheric irregularities on the L-band GEO SAR imaging. Model of GAF for GEO SAR is firstly described in Section 2, where the flowing ionospheric turbulence is included in this model. Effects of the static ionospheric irregularities on GEO SAR imaging are analyzed in Section 3, where numerical calculations and signal-level simulations are also performed. In Section 4, effects of the flowing ionospheric turbulence on the GEO SAR azimuth imaging are further studied. Finally, we draw conclusion for this paper in Section 5.

2 Model description

2.1 Original GAF formulation

Ishimaru firstly introduced GAF to describe ionospheric effects on spaceborne SAR imaging [26]. In the previous study, the SAR GAF is given by coherently processing the signals returned from the targets, which can be presented as

$$\chi(\boldsymbol{r}, \boldsymbol{r}_0) = \sum_n \frac{1}{2\pi} \int \bar{g}_n(\omega, r_n)\, \bar{f}_n^*(\omega, r_{0n})\, \mathrm{d}\omega, \tag{1}$$

where

$$\bar{f}_n^*(\omega, r_{0n}) = \bar{u}_i(\omega) \exp\{\mathrm{j}2\omega r_{0n}/c\}, \tag{2}$$

$$\bar{g}_n(\omega, r_n) = \bar{u}_i(\omega)\, \overline{G}_0(\omega, r_n), \tag{3}$$

where $\bar{u}_i(\omega)$ is the input signal, $\bar{f}_n^*(\omega, r_{0n})$ is the matched filter function focused at $\boldsymbol{r}_0$ and $\bar{g}_n(\omega, r_n)$ is the signal received at r_n due to a point target at $\boldsymbol{r}$. All above equations are defined as the Fourier transform. Therefore, GAF reaches a matched and optimal result when the target at $\boldsymbol{r}$ is precisely the reference target at $\boldsymbol{r}_0$, or else it is mismatched. $\overline{G}_0(\omega, r_n)$ is the Fourier transform of two-way Green's function and can be defined as

$$\overline{G}_0(\omega, r_n) = \frac{\exp\left\{\mathrm{j}2\int \beta(\omega)\,\mathrm{d}s + 2\psi_n\right\}}{(4\pi r_n)^2}, \tag{4}$$

where $\beta(\omega)$ is the propagation constant along the path, which includes the dispersive phase error caused by the background ionosphere, and ψ_n is the phase perturbation due to the ionospheric irregularities, which is related to the ionospheric penetration point (IPP) position. Because the ionospheric turbulence motion during the time separation between upward and downward ionospheric transitions is well below the inner-scale size for field-aligned irregularities, the down and up path phase fluctuations are reasonably equivalent [17].

2.2 Further-deduced GAF for GEO SAR

In order to obtain a further-deduced formulation of GAF, we suppose that the slant range history for every target in the scene have uniform configurations, due to the fact that it makes negligible contributions to analytical results. Meanwhile, neglecting the coupling characteristic of the GEO SAR signal between azimuth and range dimension, we can obtain an approximate formulation as

$$\bar{f}_n^*(\omega) \approx \bar{u}_i(\omega) S_{\mathrm{a}}^*(\eta_n), \tag{5}$$

$$\bar{g}_n(\omega, r, \eta) \approx \bar{u}_i(\omega) S_{\mathrm{a}}(\eta_n - \eta) \exp\{-\mathrm{j}2r\omega/\mathrm{c}\} \exp\{2\mathrm{j}(\varphi + \psi_n)\}, \tag{6}$$

where $S_{\mathrm{a}}^*(\eta_n)$ is the conjugated azimuth signal versus the azimuth instant, r is the range separation between the target at $\boldsymbol{r}$ and the reference target, and η is the azimuth temporal separation of the two targets. During the azimuth temporal separation, the ground distance scanned by the radar beam from one target to another is defined as azimuth separation, which can be formulated by $x = v_{\mathrm{g}}\eta$, where v_{g} is the ground velocity. A fourth-order model of the slant range history will be applied in the following derivations, which is generally consistent with the most conditions for GEO SAR [4]. Then, the azimuth signal can be defined as

$$S_{\mathrm{a}}(\eta_n) = W(\eta_n) \exp\left\{-\mathrm{j}2\left(R_0 + k_1\eta_n + k_2{\eta_n}^2 + k_3{\eta_n}^3 + k_4{\eta_n}^4\right)\omega_{\mathrm{c}}/\mathrm{c}\right\}, \tag{7}$$

where $W(\cdot)$ signifies the azimuth envelope, ω_{c} is the central angular frequency, R_0 is the central distance of the reference target, and $k_1 - k_4$ are the 1st to 4th order coefficients of the polynomial approximation of the slant range history. Moreover, ionospheric effects are included in (6), where ψ_n is the phase perturbation regarding the IPP position due to the ionospheric irregularities, and φ is the dispersive phase advance caused by the background ionosphere, which is given by

$$\varphi = -\frac{4\pi \cdot 40.28}{\mathrm{c}f}\mathrm{TEC_S}, \tag{8}$$

where $\mathrm{TEC_S}$ is the total electron content along the slant-range path.

If the dispersive characteristic of the ionospheric irregularities is neglected, as performed in [26, 27], GAF can be simplified and rewritten by a product of the azimuth and range GAFs,

$$\chi(r, x) = \chi_a(x) \cdot \chi_r(r), \tag{9}$$

where

$$\chi_a(x) = \sum_n \exp\{2\mathrm{j}\psi(\rho_n)\} S_{\mathrm{a}}\left(\eta_n - \frac{x}{v_{\mathrm{g}}}\right) {S_{\mathrm{a}}}^*(\eta_n), \tag{10}$$

$$\chi_r(r) = \int |\bar{u}_i(\omega)|^2 \exp\{\mathrm{j}\varphi\} \exp\{-\mathrm{j}2r\omega/\mathrm{c}\}\, \mathrm{d}\omega. \tag{11}$$

The second-moment of GAF is introduced to be a description of the imaging resolution. The background ionospheric effects on range-imaging have been comprehensively studied in [20, 21]; thus we will not expand it. Moreover, the ray-bending effect is assumed to be neglected [28]. In order to operate a quantitive analysis the azimuth resolution of SAR imaging, the second moment of the azimuth GAF for GEO SAR is given by

$$\left\langle |\chi_a(x)|^2 \right\rangle = \sum_m \sum_n \Gamma_1(\rho_n, \rho_m) {S_{\mathrm{a}}}^*(\eta_n) S_{\mathrm{a}}\left(\eta_n - \frac{x}{v_{\mathrm{g}}}\right) S_{\mathrm{a}}(\eta_n) {S_{\mathrm{a}}}^*\left(\eta_n - \frac{x}{v_{\mathrm{g}}}\right), \tag{12}$$

where $\langle\cdot\rangle$ is the mathematical expectation, and $\Gamma_1(\rho_n,\rho_m)$ can be denominated as the two-position coherence function (TPCF) to characterize the non-dispersive irregularities. TPCF can be defined as

$$\Gamma_1(\rho_n,\rho_m)=\langle\exp\{2\mathrm{j}[\psi(\rho_n)-\psi(\rho_m)]\}\rangle. \tag{13}$$

The random phase caused by the ionospheric perturbation is a normally distributed and zero-mean random [28]. According to the phase-screen theory and the theorem of large numbers, one has

$$\Gamma_1(\rho_n,\rho_m)\approx\exp\left[-2\langle\psi(\rho_n)-\psi(\rho_m)\rangle^2\right]=\exp\left[4R_\psi(x_{\mathrm{iono}})-4R_\psi(0)\right], \tag{14}$$

where x_{iono} is the IPP separation, and $R_\psi(x_{\mathrm{iono}})$ is the phase autocorrelation function on the one-dimensional phase screen. Selecting a proper mechanism of the spatial phase spectrum is crucial for subsequent analyses. Ishimaru and Liu [26,27] used the two-parameter spectrum, however it was proved by Quegan [16] that contributions from irregularities of scale sizes less than the second spectrum index are small, and then the calculation of the autocorrelation function merely requires the first spectrum index. The representative mechanism is proposed by Rino [15] and its corresponding spatial phase autocorrelation function is derived as

$$R_\psi(x_{\mathrm{iono}})={r_{\mathrm{e}}}^2\lambda^2\sec\theta_n\sec\theta_m\cos\theta GC_{\mathrm{s}}L\left|\frac{x_{\mathrm{iono}}}{2q_0}\right|^{\nu-1/2}\frac{K_{\nu-1/2}(q_0x_{\mathrm{iono}})}{2\pi\Gamma(\nu+1/2)}, \tag{15}$$

where r_{e} is the classical electron radius, λ is the wavelength, θ is the incident angle at IPP position, G is the geometric enhancement factor, C_{s} is the turbulent strength, L is the ionospheric thickness, ν is half of the phase spectrum index ($p=2\nu$), q_0 is the outer-scale cutoff wave number equal to $2\pi/L_o$ (L_0 is the outer scale), $\Gamma(\cdot)$ is the Euler's Gamma function, and $K_{\nu-1/2}(\cdot)$ is the modified Bessel function. And $R_\psi(0)$ is known as the rms phase in [15] and can be obtained by evaluating the limiting form of (14) as the space separation approaches zero,

$$R_\psi(0)={r_{\mathrm{e}}}^2\lambda^2\sec\theta GC_{\mathrm{s}}L{q_0}^{-2\nu+1}\frac{\Gamma(\nu-1/2)}{4\pi\Gamma(\nu+1/2)}. \tag{16}$$

Effects of the dispersive irregularities on the range imaging have been considered with TFTPCF [28]. Then, the simplified format of (9) cannot be appropriate any more, and can be modified as

$$\chi(x,r)=\sum_n\int|\bar{u}_i(\omega)|^2\exp\{-\mathrm{j}2r\omega/c\}\exp\{2\mathrm{j}\psi(\rho_n,f)\}S_{\mathrm{a}}\left(\eta_n-\frac{x}{v_{\mathrm{g}}}\right)S_{\mathrm{a}}^*(\eta_n)\,\mathrm{d}\omega. \tag{17}$$

Its second-moment is presented as

$$\begin{aligned}\left\langle|\chi(x,r)|^2\right\rangle=&\sum_m\sum_n\int\int|\bar{u}_i(\omega_1)|^2|\bar{u}_i(\omega_2)|^2\exp\{\mathrm{j}2r(\omega_2-\omega_1)/c\}\\&\cdot\Gamma_{1,1}(\rho_n,\omega_1;\rho_m,\omega_2)S_{\mathrm{a}}^*(\eta_n)S_{\mathrm{a}}\left(\eta_n-\frac{x}{v_{\mathrm{g}}}\right)S_{\mathrm{a}}(\eta_m)S_{\mathrm{a}}^*\left(\eta_m-\frac{x}{v_{\mathrm{g}}}\right)\mathrm{d}\omega_1\mathrm{d}\omega_2,\end{aligned} \tag{18}$$

where $\Gamma_{1,1}(\rho_n,\omega_1;\rho_m,\omega_2)$ is the TFTPCF regarding the space and frequency separations, which is equivalent to a windowing function of finite width the integral of (18) and can be denoted as

$$\Gamma_{1,1}(\rho_n,\omega_1;\rho_m,\omega_2)=\exp\left[4R_\psi(\Delta\omega,x_{\mathrm{iono}})-2R_\psi(\omega_1,0)-2R_\psi(\omega_2,0)\right], \tag{19}$$

where $R_\psi(\omega_1,0)$ and $R_\psi(\omega_2,0)$ can be computed with (16), and $R_\psi(\Delta\omega,x_{\mathrm{iono}})$ can be given by

$$R_\psi(\Delta\omega,x_{\mathrm{iono}})={r_{\mathrm{e}}}^2\lambda_1\lambda_2\sec\theta_n\sec\theta_m\cos\theta GC_{\mathrm{s}}L\left|\frac{x_{\mathrm{iono}}}{2q_0}\right|^{\nu-1/2}\frac{K_{\nu-1/2}(q_0x_{\mathrm{iono}})}{2\pi\Gamma(\nu+1/2)}. \tag{20}$$

As to a given GEO SAR system with specific ionospheric parameters, mainly including the turbulent strength, the outer scale, and the phase spectrum index, the imaging resolution can be calculated and analyzed by using [28]

$$\frac{\langle|\chi(x,r)|^2\rangle}{\langle|\chi(x_0,r_0)|^2\rangle}=\exp(-2), \tag{21}$$

where $\langle|\chi(x,r)|^2\rangle$ takes the maximal value in the position (x_0,r_0).

2.3 GAF considering the flowing irregularities

Abovementioned analytical derivations are based on the premise that the ionospheric irregularities are time-independent. However, in fact, the fluctuation in electron density is a space-time distributed field, which can be illustrated with the use of a frequency-dependent spectrum or a time-dependent autocorrelation function. In experiments where radio traverses the ionospheric turbulence, one observes both a Doppler frequency shift and a slight broadening in the received signal [13, 14]. The former effect is produced by the convection of the scattering turbulence by the mean drifting of the system, which is the emphasis here. The latter is caused by the decay mechanism that changes the configuration of the scattering turbulence, which is a much more complicated process, and thus will not be expanded in this paper. Under the hypothesis of "frozen fields", we consider perfectly the convection velocity with no decay, and the random fluctuation in electron density then satisfies

$$\xi\left(\boldsymbol{r}, t+t'\right)=\xi\left(\boldsymbol{r}-\boldsymbol{v}_0 t', t\right), \tag{22}$$

where $\boldsymbol{v}_0$ is the convection velocity. Therefore, we can obtain the wave-number-frequency dependent spectral function and the space-time autocorrelation function [13, 14], respectively, which are given by

$$S_\xi\left(\boldsymbol{k}, \omega\right)=\Phi_\xi\left(\boldsymbol{k}\right)\cdot\delta\left(\omega+\boldsymbol{k}\cdot\boldsymbol{v}_0\right), \tag{23}$$

$$R_\xi\left(\boldsymbol{r}, t\right)=R_\xi\left(\boldsymbol{r}-\boldsymbol{v}_0 t\right). \tag{24}$$

The autocorrelation function of the phase fluctuation for the ionospheric turbulence can be derived from the autocorrelation function of the electron density by [15]

$$R_\psi\left(y\right)=r_{\mathrm{e}}^2\lambda^2\Delta z\int_{-\infty}^{\infty}R_\xi\left(y, z'\right)\mathrm{d}z'. \tag{25}$$

Combining (15), (24), and (25), the space-time autocorrelation function on the ionospheric phase screen can be given by

$$\begin{aligned}&R_\psi\left(x_{\mathrm{iono}}-v_0\cos\gamma\cdot t\right)\\&\quad=r_{\mathrm{e}}{}^2\lambda^2\sec\theta_n\sec\theta_m\cos\theta GC_{\mathrm{s}}L\left|\frac{x_{\mathrm{iono}}-v_0\cos\gamma\cdot t}{2q_0}\right|^{\nu-1/2}\frac{K_{\nu-1/2}\left(q_0\left(x_{\mathrm{iono}}-v_0\cos\gamma\cdot t\right)\right)}{2\pi\Gamma\left(\nu+1/2\right)},\end{aligned} \tag{26}$$

where t is the time separation, $v_0\cos\gamma$ is the projection velocity of the turbulence convection by the included angle with the IPP scanning direction. As to (14), the temporal-variable TPCF caused by flowing plasmas can be modified as

$$\Gamma_1\left(x_{\mathrm{iono}}-v_0\cos\gamma\cdot t\right)=\exp\left[4R_\psi\left(x_{\mathrm{iono}}-v_0\cos\gamma\cdot t\right)-4R_\psi\left(0\right)\right], \tag{27}$$

where the IPP separation x_{iono} is proportional to time separation by the factor of IPP scanning velocity, and thus Eqs. (26) and (27) can be rewritten $R_\psi\left(v_{\mathrm{eff}}t\right)$ and $\Gamma_1\left(v_{\mathrm{eff}}t\right)$, respectively. And v_{eff} is the relative velocity of the irregularities as seen by an observer in the reference coordinate system [15], which can be denoted as

$$v_{\mathrm{eff}}=v_i-v_0\cos\gamma. \tag{28}$$

Or we can also obtain a spatial autocorrelation function as

$$R_\psi\left(v_{\mathrm{eff}}t\right)=R_\psi\left(v_{\mathrm{eff}}x_{\mathrm{iono}}/v_i\right)=R_\psi\left(\beta x_{\mathrm{iono}}\right), \tag{29}$$

where β is a scale ratio between the relative velocity and the IPP scanning velocity. Although some existent researches have considered the flowing ionospheric irregularities, the flowing distance of the ionospheric turbulence can be reasonably considered to be neglected during the short integration time for the LEO SAR system [17, 18, 28]. Moreover, the turbulence convection is static compared with the much faster IPP scanning. Nevertheless, due to the particular geometric configuration with a slow IPP

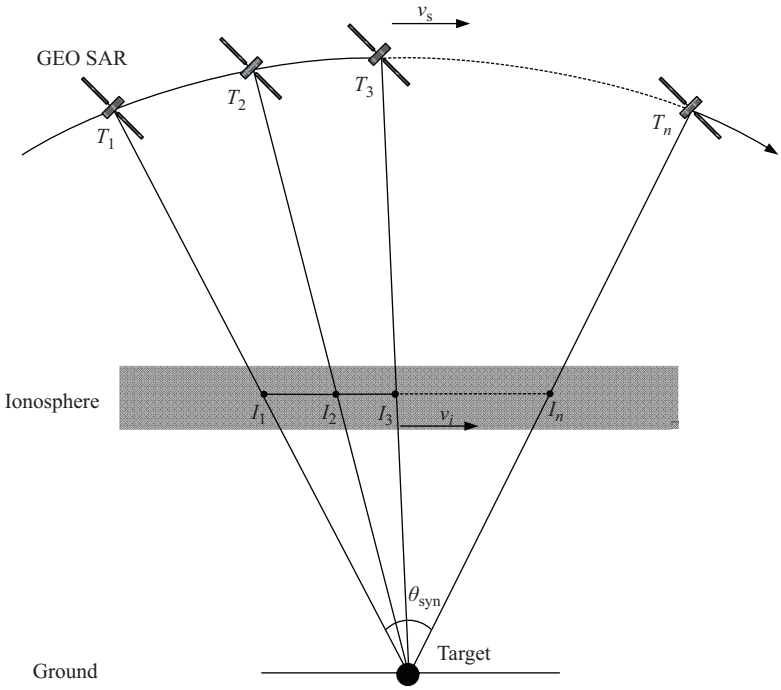

Figure 1 The geometric configuration of GEO SAR with the ionosphere.

scanning velocity and an ultra-long integration time, the static ionospheric irregularities are no longer satisfied for the GEO SAR system.

In order to interpret the turbulence convection and the IPP scanning, we illustrate the curvilinear geometry between GEO SAR and the ionosphere in Figure 1, where each azimuth instant is corresponding to an IPP at the height of the ionospheric phase screen. In Figure 1, $\theta_{\rm syn}$ is the synthetic angle, $v_{\rm s}$ is the satellite velocity, and v_i is the IPP scanning velocity. It is noted that the IPP scanning velocity is distinct from the velocity of the beam centroid scanning at the ionospheric altitude, which is approximate to the ground velocity, up to hundreds of meters per second. For a point target, we can calculate the IPP scanning velocity by

$$v_i = \frac{L_{\rm iono}}{T_a}, \tag{30}$$

where T_a is the integration time for GEO SAR, and $L_{\rm iono}$ is the length of the system's synthetic aperture at the height of the ionosphere, which denotes the length of the ionospheric penetration trajectory generated by the scanning of IPP during the integration time and can be derived as a function of the synthetic angle

$$L_{\rm iono} \approx \theta_{\rm syn} H_{\rm iono} = \frac{0.886\lambda}{2\rho_a} H_{\rm iono}, \tag{31}$$

where $H_{\rm iono}$ is the equivalent altitude of the ionospheric phase screen, which is generally assumed to be 400 km, and $\rho_{\rm a}$ is the azimuth resolution of GEO SAR.

For the typical LEO SAR system, the IPP scanning velocity reaches thousands of meters per second, while its integration time is merely several seconds; thereby the ionospheric turbulence is static. Orbit parameters of GEO SAR are provided in Table 1, which will also be applied to simulating the GEO SAR imaging resolution. If there is no special declaration, orbit parameters are acquiescent as shown in Table 1. Because both the azimuth resolution and the integration time are varying with the argument of latitude, we depict the IPP scanning velocity along the satellite position for the typical GEO SAR system in Figure 2, which is nearly independent upon the systematic parameters of GEO SAR, such as carrier frequency, integration time and azimuth resolution, but it is a function of the antenna look-down angle. As shown in Figure 2, the IPP scanning velocity is merely tens of meters per second for GEO SAR, approximating to 30 m/s in the equatorial region. It was reported that the convection velocity was

Table 1 Orbit parameters of GEO SAR

Parameter	Specification
Semi-major axis	42164.17 km
Eccentricity	0
Inclination	60°
Right ascension of ascending node	115°
Argument of perigee	270°
Argument of latitude	0°

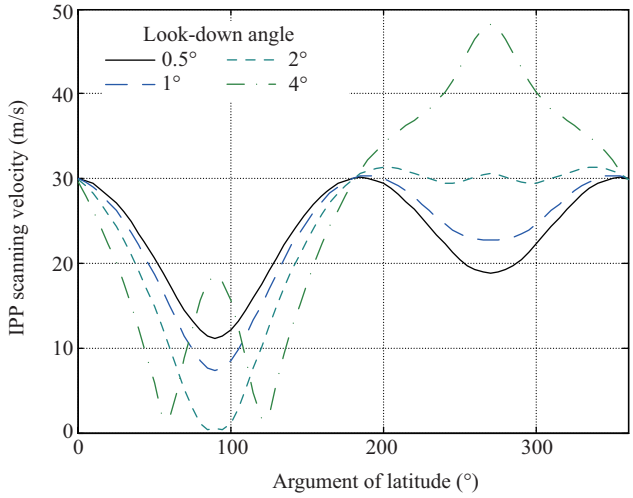

Figure 2 (Color online) The IPP scanning velocity of GEO SAR.

up to 100 m/s in the equatorial region [17], which was comparable for the IPP scanning velocity of GEO SAR. Therefore, the ionospheric turbulence is not static any longer for GEO SAR, which is necessary to be considered when we analyze the imaging resolution.

3 Effects of static ionospheric turbulence on GEO SAR imaging

In this section, we discuss the effects of static ionospheric turbulence on GEO SAR imaging, which means the convection velocity of the ionospheric eddies is assumed to be zero or normal to the IPP scanning direction, and then $\beta = 1$.

3.1 Numerical study

Numerical calculations of the TFTPCF for the typical L-band system (1.25 GHz) will be firstly given. We investigate the vertical integrated strength of turbulence at the 1 km scale C_kL to quantitively characterize the turbulent strength, which is generally known as the scintillation strength and given by $C_kL = C_sL(\frac{2\pi}{1000})^{-(2\nu+1)}$ [17,18]. As shown in (15), the rms phase is proportional to C_kL, which means the phase fluctuation intensifies with the increase of C_kL. Thus, we take the $\log_{10}(C_kL) = 31, 32, 33, 34$ into account, which indicate the classic values of the weak, moderate, heavy and terribly heavy scintillation phenomena, respectively. We assume that the equivalent ionospheric thickness is 50 km, the antenna look-down angle is 4°, the phase spectrum index is 3, and the outer scale is normally set to 10 km. Figure 3(a) and (b) present the resulting TFTPCFs versus space and frequency separations for different values of C_kL, respectively. Results show that the ionospheric irregularities change the spatial coherence seriously, which means that the azimuth resolution is severely exacerbated in the condition of the intensive ionospheric destabilization. It can be seen that the decorrelation caused by the frequency separation is negligible compared with that of the position separation. This means that the dispersive feature of

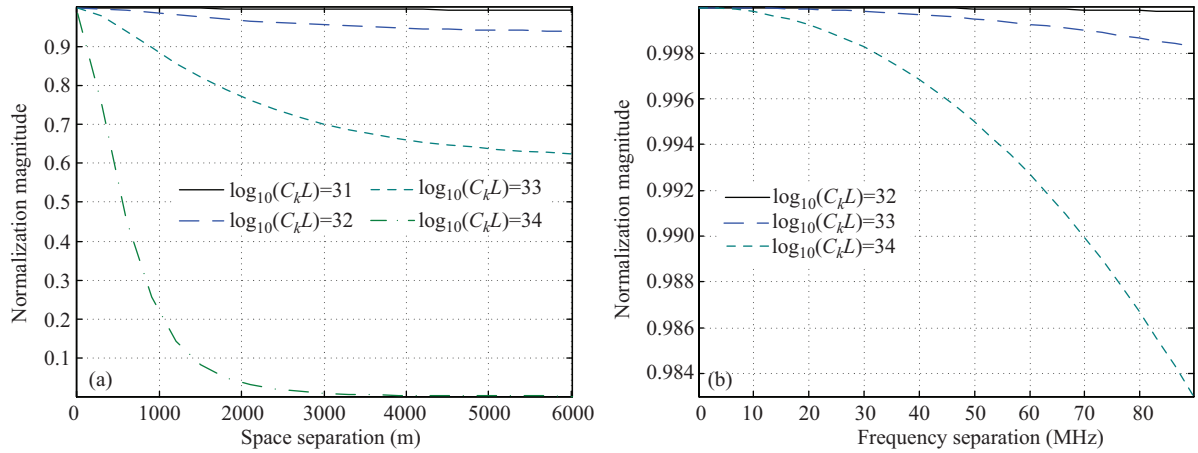

Figure 3 (Color online) TFTPCF for different values of C_kL. (a) TFTPCF versus space separation; (b) TFTPCF versus frequency separation.

ionospheric irregularities can be reasonably neglected, and thus the range imaging of GEO SAR will not be distorted. This conclusion will be further validated by the following simulation analyses.

Furthermore, we select two groups of parameters to go on, each group including the integrated time and systematic bandwidth for the L-band GEO SAR system: [100 s, 20 MHz] and [200 s, 40 MHz]. Along with the system parameters in Table 1, we assume the argument of latitude is 0°, which will be also applied to subsequent numerations and simulations; it means the satellite just flies over the equator. On the basis of the TFTPCF model and Rino's spectral mechanism, the imaging resolutions are measured via the second-moment GAF. Acquiescent ionospheric parameters are presumed without the special declaration: $p = 3$, $L_o = 10$ km, and $C_kL = 10^{33}$; two of the ionospheric parameters is fixed to study the other parameter's effect on the imaging resolution, based on that p ranges from 2 to 6, L_o ranges from 1 km to 100 km, and C_kL generally ranges from 10^{30} to 10^{36}.

Figures 4–6 exhibit simulation results of the imaging resolution changed with the spectrum index, the outer scale and the scintillation strength, respectively. It is proved that the broadening ratio in range-imaging resolution is less than five per cent even on the condition of the intensive ionospheric destabilization, and then can be negligible, which is a good agreement with the above simulation of TFTPCF; thereby TFTPCF can be reasonably degraded with TPCF for a brief format of GAF in (9). For GEO SAR with a better azimuth resolution, it is more susceptible to the ionospheric irregularities. In the case of the extremely instable ionospheric perturbation, it tends to be independent upon the original resolution, but dependent on the ionospheric scintillation parameters. Moreover, it can also be concluded that the scintillation strength makes much greater contributions to the imaging deterioration than the other two; thus we next take the scintillation strength into account for the description of the ionospheric irregularities.

3.2 Monte Carlo simulations

In the preceding subsection, effects of static ionospheric turbulence on the GEO SAR imaging resolution have been analyzed via the numerical calculation of the second-moment GAF. Signal-level simulations are carried out to further validate the above-mentioned numerical analyses. We select an L-band GEO SAR system with the integration time of 100 s and the range bandwidth of 20 MHz. C_kL generally ranges from 10^{30} to 10^{36}, and other two ionospheric parameters are fixed to acquiescence. Based on the phase screen theory, corresponding echo data influenced by the ionospheric irregularities are generated, which can be focused with the RD-ACS imaging algorithm [4]. Monte Carlo simulations repeating one hundred times are applied to averaging all the amplitude images. Statistic results of the imaging resolution and peak power are obtained and shown in Figure 7, where numerical calculation results are also illustrated for contrast. It is proved that simulation results are highly uniform with numerical calculations, which verifies the theoretical model.

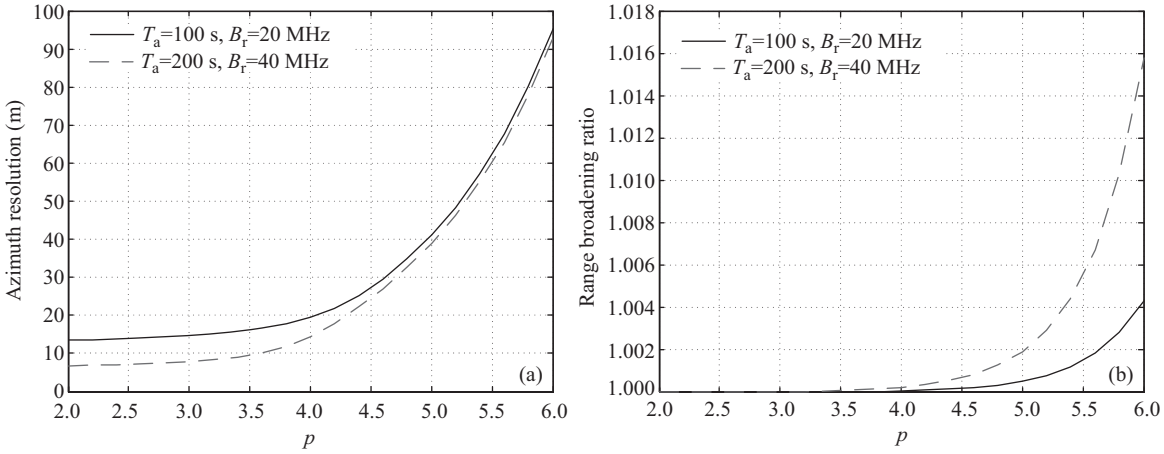

Figure 4 Imaging resolution changed with the spectrum index. (a) Azimuth; (b) range.

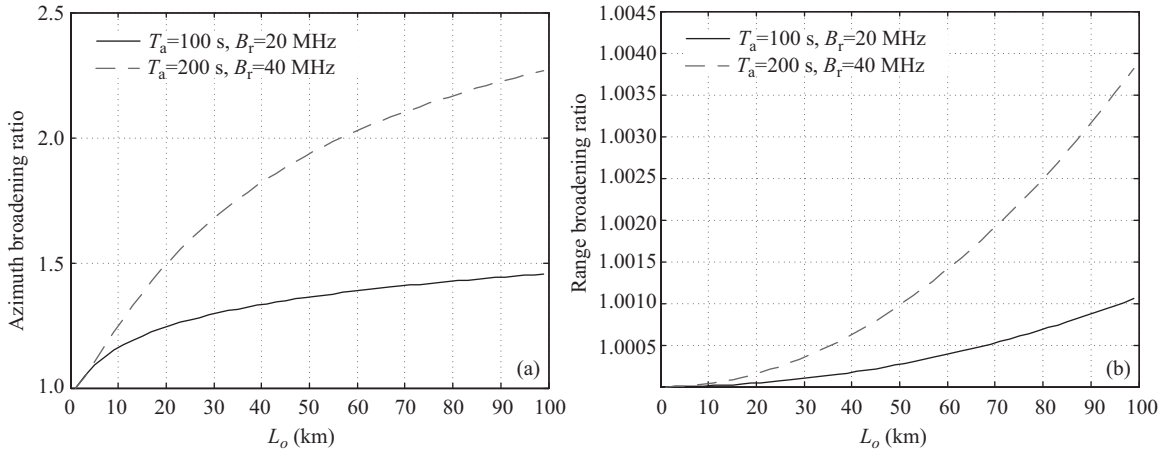

Figure 5 Imaging resolution changed with the outer scale. (a) Azimuth; (b) range.

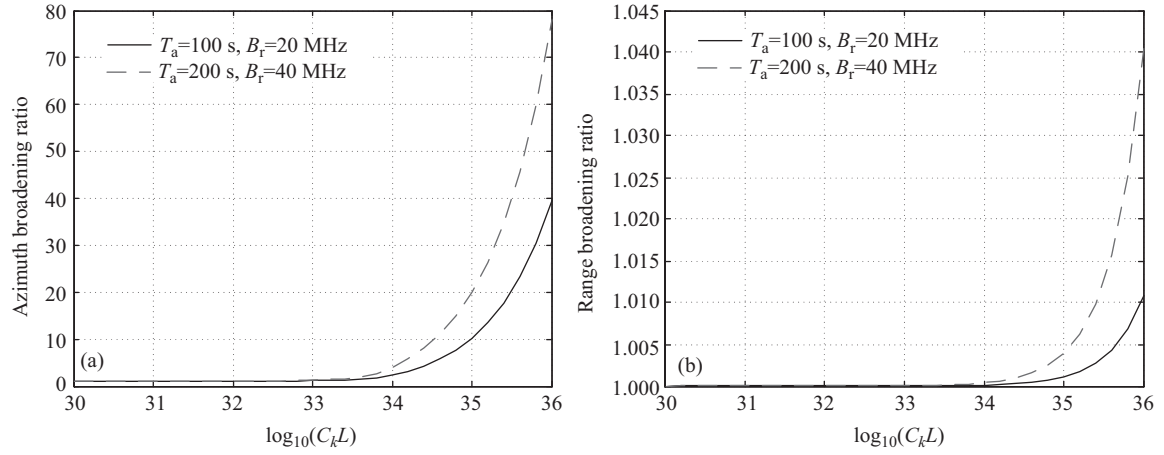

Figure 6 Imaging resolution changed with the scintillation strength. (a) Azimuth; (b) range.

4 Effects of flowing ionospheric turbulence on GEO SAR azimuth imaging

Systematic and ionospheric parameters are listed in Table 2 for subsequent numerical and simulative study. Ionospheric turbulence convection will be taken into account in this section, where the analysis of range-imaging resolution will not be covered because its deterioration has been proved to be negligible

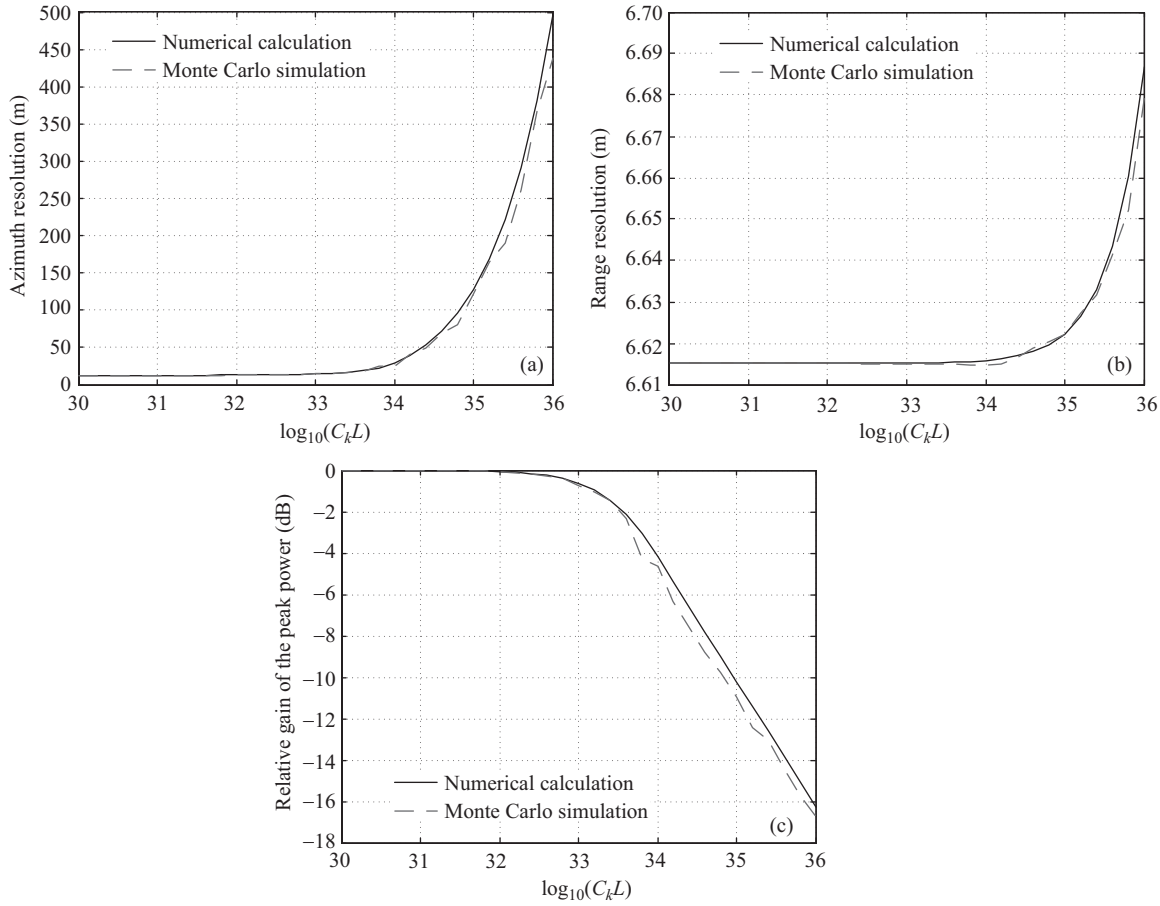

Figure 7 Monte Carlo simulation results compared with the theoretical numeration. (a) Azimuth resolution; (b) range resolution; (c) peak power.

for the L-band GEO SAR system; it is also an additional advantage of reducing the data dimension. Without the loss of generality, TPCF versus time separation formulated by $\Gamma_1(v_{\text{eff}}t)$ is illustrated in Figure 8, which is a function of the relative velocity. It has been accepted that if the coherent duration is less than the integration time of GEO SAR, the azimuth-imaging resolution is obviously deteriorated. In the case that the relative velocity tends to zero, IPP is equivalent to a constant point and the ionospheric irregularities have no influence on GEO SAR imaging in theory. And it is the original condition of static ionospheric turbulence discussed in Section 3, in the case of $v_{\text{eff}} = 30$ m/s. It can be seen from Figure 8 that the azimuth decorrelation during the integration time will be intensified with the increasing of the relative velocity. According the systematic and ionospheric parameters listed in Table 2, we operate theoretical numerations and Monte Carlo simulations repeating one hundred times, the results of which are shown in Figure 9. It reveals that the deterioration severity of the azimuth-imaging resolution for GEO SAR is positively correlated to the relative velocity. Moreover, theoretical numeration is highly consistent with Monte Carlo simulation, which verifies the theoretical model. In following simulations, we assume an approximate ionospheric convection velocity of 100 m/s along the geographic west or geomagnetic east direction, and this approximation is based on typical flowing velocities measured at Kwajalein ($8°43'\text{N}, 167°44'\text{E}$), which can be taken as the typical equatorial region [17]. According to the geometric configuration of GEO SAR, we can calculate the included angle between the ionospheric convection and IPP scanning, which approximates to 60°; therefore, the relative velocity is 20 m/s, which can be computed by (28). Based on the parameters summarized in Table 2, Monte Carlo simulation result of azimuth profile of the point target is shown in Figure 10(a), where we also illustrate the results of $v_{\text{eff}} = 0$ and $v_{\text{eff}} = 100$ m/s for comparison. Azimuth profiles of one realization are given in Figure 10(b). It further proves that the GEO SAR system with a higher relative velocity has a worse

Table 2 Systematic and ionospheric parameters of GEO SAR

Parameter	Specification
Carrier frequency	1.25 GHz
Antenna look-down angle	4°
Integration time	100 s
Ideal azimuth resolution	12.53 m
IPP scanning velocity	30 m/s
Outer scale	10 km
Spectrum index	3
Scintillation strength	10^{33}
Convection velocity of the ionospheric irregularities	100 m/s

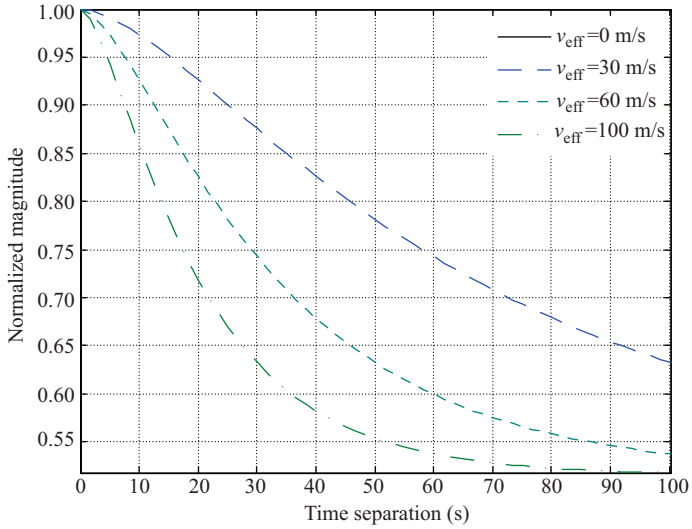

Figure 8 (Color online) TPCF versus time separation for different relative velocities.

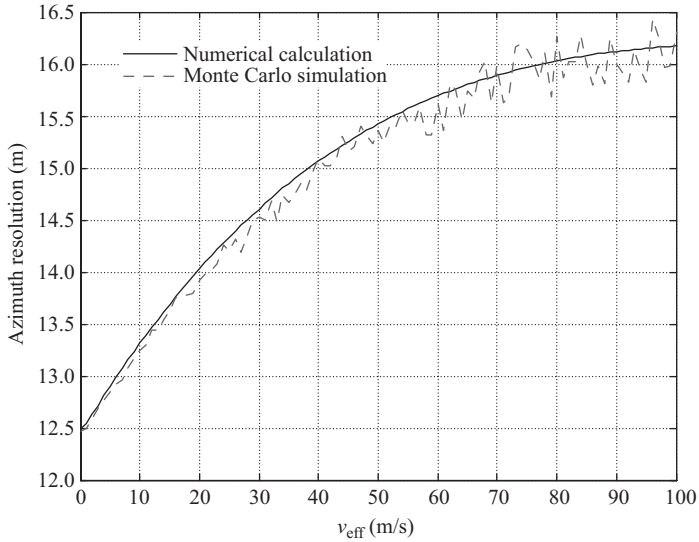

Figure 9 Azimuth imaging resolutions versus the relative velocities operated via theoretical numeration and Monte Carlo simulation.

imaging resolution. In reality, given systematic and ionospheric parameters and the concrete geometric configuration of GEO SAR with the ionosphere, effects of the ionospheric turbulence on GEO SAR imaging resolution can be concretely evaluated.

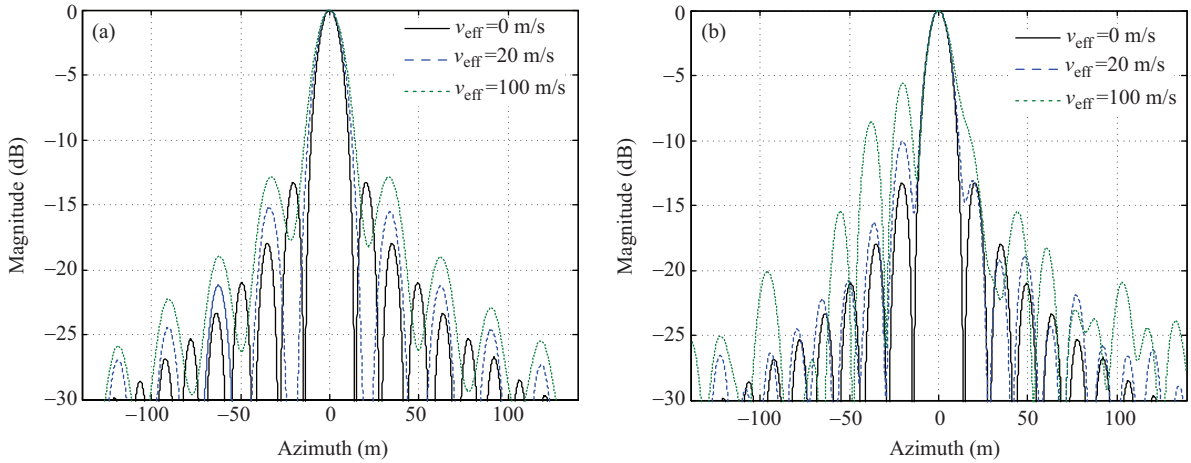

Figure 10 (Color online) Azimuth profiles for different relative velocity. (a) Monte Carlo simulations; (b) one realization.

5 Conclusion

This paper presents a theoretical analysis of ionospheric irregularities effects on L-band GEO SAR imaging using GAF. Based on the phase-screen theory and Rino's spectral mechanism, analytical models of TPCF and TFTPCF have been derived to describe the ionospheric irregularities. Both the time-independent and flowing ionospheric turbulences are considered. The theoretical and simulation results indicate that effects of the ionospheric irregularities on range resolution can be neglected for the L-band GEO SAR system and the scintillation strength plays a dominant role in the azimuth-imaging resolution. Furthermore, the deterioration severity of the azimuth-imaging resolution is positively correlated to the relative velocity of the irregularities as seen by an observer in the reference coordinate system. Analytical results presented in this paper will be useful for studying associated compensation methods. In the near future, an in-depth analysis will be operated to study the flowing ionospheric turbulence with the complex decay mechanism.

Acknowledgements This work was supported by National Natural Science Foundation of China (Grant Nos. 41271459, 61501477).

Conflict of interest The authors declare that they have no conflict of interest.

References

1 Tomiyasu K, Pacelli J L. Synthetic aperture radar imaging from an inclined geosynchronous orbit. IEEE Trans Geosci Remote Sens, 1983, 21: 324–329
2 Hu C, Long T, Zeng T, et al. The accurate focusing and resolution analysis method in geosynchronous SAR. IEEE Trans Geosci Remote Sens, 2011, 49: 3548–3563
3 Hu C, Liu Z P, Long T. An improved CS algorithm based on the curved trajectory in geosynchronous SAR. IEEE J Sel Topics Appl Earth Observ Remote Sens, 2012, 5: 795–808
4 Li D X, Wu M Q, Sun Z Y, et al. Modeling and processing of two-dimensional spatial-variant geosynchronous SAR data. IEEE J Sel Topics Appl Earth Observ Remote Sens, 2015, 8: 3999–4009
5 Zeng T, Yin W, Ding Z G, et al. Motion and Doppler characteristics analysis based on circular motion model in geosynchronous SAR. IEEE J Sel Topics Appl Earth Observ Remote Sens, 2016, 9: 1132–1142
6 Hu C, Tian Y, Zeng T, et al. Adaptive secondary range compression algorithm in geosynchronous SAR. IEEE J Sel Topics Appl Earth Observ Remote Sens, 2016, 9: 1397–1413
7 Chen J L, Sun G C, Xing M D, et al. A parameter optimization model for geosynchronous SAR sensor in aspects of signal bandwidth and integration time. IEEE Geosci Remote Sens Lett, 2016, 13: 1374–1378
8 Ding Z G, Shu B Z, Yin W, et al. A modified frequency domain algorithm based on optimal azimuth quadratic factor compensation for geosynchronous SAR imaging. IEEE J Sel Topics Appl Earth Observ Remote Sens, 2016, 9: 1119–1131
9 Dong X C, Hu C, Tian W M, et al. Feasibility study of inclined geosynchronous SAR focusing using Beidou IGSO signals. Sci China Inf Sci, 2016, 59: 129302
10 Xu Z W, Wu J, Wu Z S. A survey of ionosphere effects on space-based radar. Waves Random Media, 2004, 14: 189–273
11 Belcher D P. Theoretical limits on SAR imposed by the ionosphere. IET Radar Sonar Navig, 2008, 2: 435–448

12 Li L, Zhang Y S, Dong Z. Ionospheric polarimetric dispersion effect on low-frequency spaceborne SAR imaging. IEEE Geosci Remote Sens Lett, 2014, 11: 2163–2167
13 Shkarofsky I P. Turbulence functions useful for probes and for scattering analysis. Can J Phys, 1968, 46: 2683–2702
14 Yeh K C, Liu C H. Radio wave scintillations in the ionosphere. Proc IEEE, 1982, 70: 324–360
15 Rino C L. A power law phase screen model for ionospheric scintillation 1. Weak Scatter Radio Sci, 1979, 14: 1135–1145
16 Quegan S, Lamont J. Ionospheric and tropospheric effects on the synthetic aperture radar performance. Int J Remote Sens, 1986, 7: 525–539
17 Neil C R, Paul S C, Keith M G. Measurements and simulation of ionospheric scattering on VHF and UHF radar signals: channel scattering function. Radio Sci, 2009, 44: 1–10
18 Charles S C, Keith M G, Ronald G C. Simulating the impacts of ionospheric scintillation on L band SAR image formation. Radio Sci, 2012, 47: 1–14
19 Wang C, Zhang M, Xu Z W, et al. Cubic phase distortion and irregular degradation on SAR imaging due to the ionosphere. IEEE Trans Geosci Remote Sens, 2015, 53: 3442–3451
20 Tian Y, Hu C, Dong X C, et al. Theoretical analysis and verification of time variation of background ionosphere on geosynchronous SAR imaging. IEEE Geosci Remote Sens Lett, 2015, 12: 721–725
21 Hu C, Tian Y, Yang X P, et al. Background ionosphere effects on geosynchronous SAR focusing: theoretical analysis and verification based on the BeiDou navigation satellite system (BDS). IEEE J Sel Topics Appl Earth Observ Remote Sens, 2016, 9: 1143–1162
22 Li Y H, Hu C, Dong X C, et al. Impacts of ionospheric scintillation on geosynchronous SAR focusing: preliminary experiments and analysis. Sci China Inf Sci, 2015, 58: 109301
23 Hu C, Li Y H, Dong X C, et al. Avoiding the ionospheric scintillation interference on geosynchronous SAR by orbit optimization. IEEE Geosci Remote Sens Lett, 2016, 13: 1676–1680
24 Dong X C, Hu C, Tian Y, et al. Experimental study of ionospheric impacts on geosynchronous SAR using GPS signals. IEEE J Sel Topics Appl Earth Observ Remote Sens, 2016, 9: 2171–2183
25 Hu C, Li Y H, Dong X C, et al. Performance analysis of L-band geosynchronous SAR imaging in the presence of ionospheric scintillation. IEEE Trans Geosci Remote Sens, 2017, 55: 159–172
26 Ishimaru A, Kuga Y, Liu J, et al. Ionospheric effects on synthetic aperture radar at 100 MHz to 2 GHz. Radio Sci, 1999, 34: 257–268
27 Liu J, Kuga Y, Ishimaru A, et al. Ionospheric effects on SAR imaging: a numerical study. IEEE Trans Geosci Remote Sens, 2003, 41: 939–947
28 Li L L, Li F. SAR imaging degradation by ionospheric irregularities based on TFTPCF analysis. IEEE Trans Geosci Remote Sens, 2007, 45: 1123–1130
29 Xu Z W, Wu J, Wu Z S. Potential effects of the ionosphere on space-based SAR imaging. IEEE Trans Antennas Propag, 2008, 56: 1968–1975
30 Wang C, Zhang M, Xu Z W, et al. Effects of anisotropic ionospheric irregularities on space-borne SAR imaging. IEEE Trans Antennas Propag, 2014, 62: 4664–4673